Regulating the Superficial Vacancies and OH⁻ Orientations on Polarized Hydroxyapatite Electrocatalysts

Jordi Sans, Marc Arnau, Francesc Estrany, Pau Turon* and Carlos Alemán**

J. Sans, M. Arnau, Dr. F. Estrany, Prof. C. Alemán
Departament d'Enginyeria Química, EEBE, Universitat Politècnica de Catalunya, C/ Eduard Maristany, 10-14, Ed. I2, 08019, Spain
E-mail: jordi.sans.mila@upc.edu and carlos.aleman@upc.edu

J. Sans, M. Arnau, Dr. F. Estrany, Prof. C. Alemán
Barcelona Research Center in Multiscale Science and Engineering, Universitat Politècnica de Catalunya, C/ Eduard Maristany, 10-14, 08019, Barcelona, Spain

Dr. P. Turon
B. Braun Surgical, S.A.U. Carretera de Terrassa 121, 08191 Rubí (Barcelona), Spain
E-mail: pau.turon@bbraun.com

Prof. C. Alemán
Institute for Bioengineering of Catalonia (IBEC), The Barcelona Institute of Science and Technology, Baldiri Reixac 10-12, 08028 Barcelona Spain

Abstract. Smart designs of hydroxyapatite (HAp) materials with customized electrical properties are drawing increasing attention for their wide range of potential applications. Such enhanced electrical properties directly arise from the number and orientation of OH⁻ groups in the HAp lattice. Although different polarization treatments have been proposed to enhance the final conductivity by generating vacancies at high temperatures and imposing specific OH⁻ orientations through electric voltages, no direct measurement showing the evolution that OH⁻ groups undergo has been described yet. In this article, we report the first direct empirical observation that allows the characterization of both the generation of vacancies and the polarization of OH⁻ groups. The mechanisms behind the electrical enhancement have been elucidated allowing to distinguish between charge accumulation at the crystal grains, which is due to the formed vacancies, and charge accumulation in the boundaries of particles. In addition, a linear dependence between the number of vacancies and the superficial charge has been observed. Therefore, it has been demonstrated that the charge accumulation at the

micrometric grain boundaries has a great impact on the catalytic properties of the thermally stimulated polarized HAp. These results will be used for further optimization of the catalyst properties.

1. Introduction

Synthetic hydroxyapatite (HAp) is the foremost versatile and widely used ceramic for both biomedical and technological purposes.[1] A great deal of effort has been put into developing customized HAp-based materials with reinforced properties to fulfill the requirements of specific applications.[2,3] Within this context, the ability to control the electrical properties of HAp is attracting increased attention, as those properties not only have demonstrated to play a crucial role in tissue engineering[4] and smart bioengineering[5] but also to open the way for other uses, such as electronics[6] and green catalysis.[7,8].

The electrical properties of HAp arise directly from the OH$^-$ ions contained in its crystal lattice who can be treated as dipoles arranged in parallel columns aligned with the c-axis. Enhanced electrical conductivities were successfully achieved at high temperatures by generating OH$^-$ vacancies due to a dehydration process that was described as follows:[9,10]

$$Ca_{10}(PO_4)_6(OH)_2 \rightarrow Ca_{10}(PO_4)_6(OH)_{2-2x}O_x\Delta_x + {}_xH_2O \qquad (1)$$
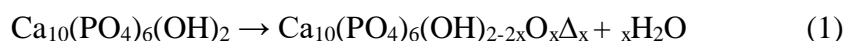
where Δ denotes OH$^-$ vacancies. Although the generation of vacancies was measured *in situ* by Raman microscopy,[11] the posterior effect of this treatment at room temperature has not been reported yet. Such dehydration process, hereafter denoted *calcination* treatment, is also responsible for structural changes, affecting the crystallinity and mechanical properties of HAp.[12,13] Low generation of vacancies and suppression of carbonates present in the crystal lattice is expected to cause an increment of the crystallinity. Conversely, fast generation of vacancies, which can be favored by OH$^-$ abundant atmospheres at high temperatures, generates disorder or even transitions to other calcium phosphate salts, such as amorphous calcium phosphate (ACP) or β-tricalcium phosphate (βTCP), altering the final properties of

HAp.[12] Additionally, the higher the number of vacancies, the higher the mobility of OH$^-$ dipoles that are less effected by the electrostatic forces of nearby OH$^-$ in the same column.[14]

Control of the orientation of OH$^-$ groups is highly desirable to stabilize the mineral and its properties. Therefore, a treatment consisting in imposing a defined global OH$^-$ orientation has been developed by means of a polarization treatment at high temperature, which has been denoted *thermally-stimulated polarization* (TSP).[15-17] In this approach, the disorder is reduced and the OH$^-$ columns act as quantum pathways for drastically increased electron transport, creating space charge accumulation at the crystal grain boundaries.[10,18] In a recent study, we reported for the first time a highly stable and permanently polarized HAp with considerably enhanced electrical properties at room temperature, proving that the conditions of voltage and temperature applied during the TSP treatment were crucial.[16] Although the effect of the TSP treatment on HAp has been studied in terms of bulk by analyzing the resultant enhanced electrical properties,[10,15,16,18,19] fundamental studies on the evolution of the OH$^-$ ions after both dehydration process and TSP treatment have not been reported yet. This is an important drawback for optimizing the TSP process parameters and for demonstrating experimentally those previously hypothesized mechanisms about the spatial orientation of the OH$^-$ groups and their implications on the electrical properties.

Direct observation and characterization of OH$^-$ dipoles are complex issues, which have only been addressed experimentally considering dielectric relaxations.[20] In this work, for the first time we successfully link the electrical properties of HAp with the direct experimental measurements of OH$^-$ groups. Thus, optimization and discernment of critical parameters, such as the generation of vacancies and the crystallinity, have been studied to elucidate the mechanism behind the TSP treatment. Additionally, we present atomic force microscopy (AFM) as a suitable technique for characterizing the nanosurface after TSP treatment. Finally, the implications of the TSP treatment in the catalytic activity of permanently polarized HAp are discussed.

2. Results and Discussion

2.1. Effect of Time and Temperature on Vacancies Generation

Structural characterization of calcined samples is challenging, as it involves changes in the crystallinity and lattice modifications, normally measured by WAXD or neutron diffraction. However, we recently demonstrated that Raman microscopy is a useful technique to quantify the relative amount of OH⁻ groups in HAp and to measure interesting crystal lattice parameters, such as crystallinity or phase distribution.[12]

Raman spectra of non-calcined HAp samples (HAp-25) and calcined at 1000 ℃ (HAp-1000), which are displayed in **Figure 1a**, exhibit the characteristic HAp peaks that correspond to the P–O vibrations at $\nu_1 = 962$ cm^{-1}, $\nu_2 = 400\text{-}480$ cm^{-1}, $\nu_3 = 570\text{-}625$ cm^{-1} and $\nu_4 = 1020\text{-}1095$ cm^{-1}, and the stretching vibration of ν–OH at 3574 cm^{-1}.[21] This work focuses on monitoring the evolution of the OH⁻ groups and, therefore, the 532 nm laser has been employed. This is because the 532 nm laser enhances the sensitivity sensitivity of the hydroxyl vibration in comparison to the standard 785 nm laser (Figure S1). However, the utilization of the 532 nm laser easily promotes fluorescence and phosphorescence phenomena, causing a lowering of the signal to noise ratio, as is illustrated in Figure S2 for HAp-25.

Complementary FTIR studies (Figure S3) revealed the presence of carbonates (well-defined bands at 1330, 1420 and 1648 cm^{-1}) and water (wide band at 3400 cm^{-1}),[22] which are responsible of the above mentioned phenomena. These species completely evaporate during the calcination treatment, explaining the optimum signal to noise ratio observed for HAp-1000. Careful inspection of the ν-OH (Figure 1b) and ν_1 (Figure 1c) regions in the Raman spectra confirms the generation of OH⁻ vacancies and the increment of crystallinity due to the calcination treatment. Indeed, the hydroxyl content (A_{OH}), which was determined as the ratio

of the integrated peaks at 3574 and 962 cm^{-1}, decreased from 0.25 for HAp-25 to 0.16 for HAp-1000.
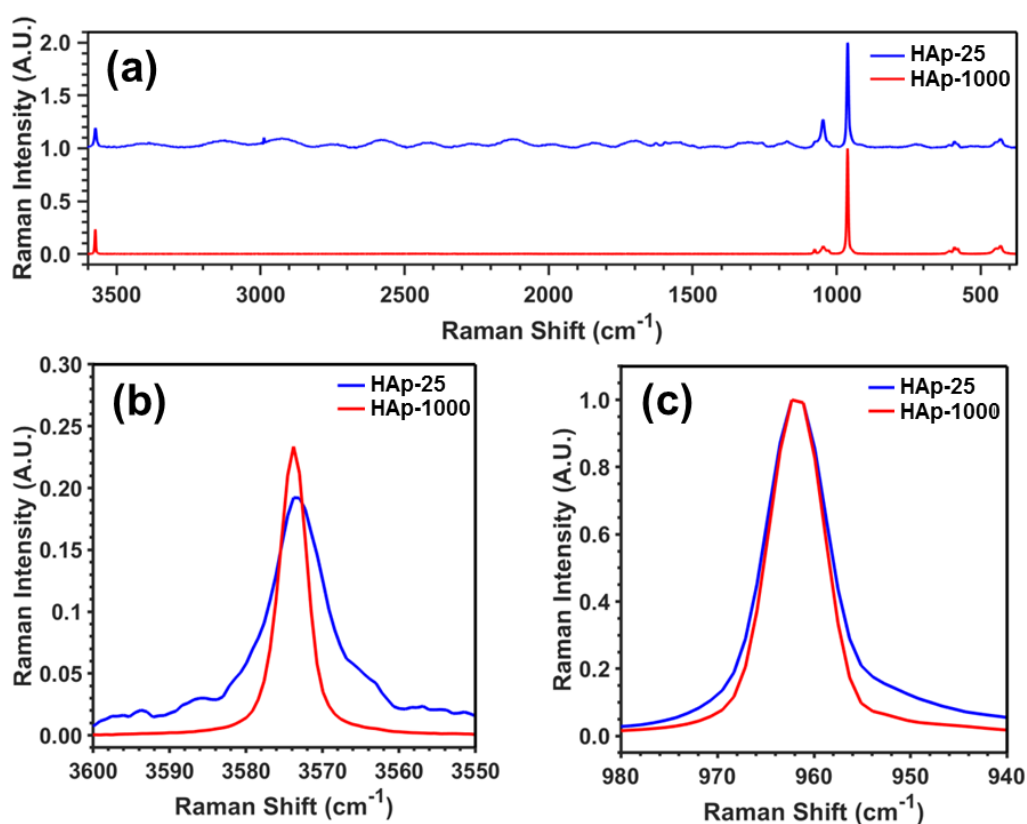
Figure 1. (a) Raman spectra of HAp-25 and HAp-1000 samples using the 532 nm laser for v-OH enhancement. Magnification of the regions comprised between (b) 3550 – 3600 cm^{-1} (v-OH) and (c) 940 – 980 cm^{-1} (v_1). Magnified spectra were used to evaluate I_{OH}, A_{OH}, FWHM and $FWHM_{OH}$.

The crystallinity was determined from the variation of the full width at half maximum (FWHM) of the main peak v_1, which is 7.1 and 6.5 cm^{-1} for HAp-25 and HAp-1000, respectively. A narrowing of all peaks is expected when the crystallinity is enhanced. This is reflected for HAp-1000, in which all the vibrational modes are well-resolved, including the O–P–O bending vibration v_4 at 1076 cm^{-1}. However, the ratio between the FWHM of the 3574 and 962 cm^{-1} peaks ($FWHM_{OH}$) is not maintained for HAp-25 and HAp-1000 samples, presenting a slight decrease for HAp-1000 (*i.e.* 1.1 and 0.7 for HAp-25 and HAp-1000, respectively). This indicates that the remaining OH$^-$ groups have fewer defects than the rest of the species. Consistently, the ratio between the intensity of the 3574 cm^{-1} and 962 cm^{-1} peaks

(I_{OH}) increases from 0.16 to 0.23 due to the total energy conservation, although the final

difference between the intensities decreases as a result of the vacancy generation. Finally, the

presence of other calcium phosphate salts, which is usual in samples prepared by chemical

precipitation, is not detected, as they appear in the form of a shifting or splitting of the ν_1 main

peak.[22,23] Accordingly, the prepared samples are highly pure in HAp content. In order to

generalize this effect, HAp presenting distinct degrees of crystallinity has been analyzed

(Figure S4 and Table S1), obtaining similar behaviors (Figure S5).

Figure 2a-c shows the structural characterization of calcined HAp as a function of the

calcination temperature. The generation of vacancies (A_{OH}) and the crystallinity (I_{OH},

$FWHM_{OH}$ and FWHM) increase progressively with the calcination temperature. The optimum

calcination temperature is 900 and 1000 ºC for the generation of vacancies and crystallinity,

respectively. Moreover, two different regimes are clearly observed as a function of calcination

temperature interval, suggesting the existence of two different phenomena. For calcination

temperatures up to 600-700 ºC all the analyzed parameters present a linear behavior, whereas

a discontinuity followed by an exponential decreasing regime appears at higher temperatures.

Vacancies in the crystal lattice act as reversal points from which OH⁻ groups can reorient,

minimizing their electrostatic forces and leading to further stabilization of the HAp hexagonal

phase.[14,24] Accordingly, it is reasonable to assume that the generation of vacancies is

energetically favored and increases the crystallinity until the number of reversal points in the

lattice is high enough to compensate the steric forces.

The OH⁻ groups experience small changes in their orientation when the calcination

temperature is ≤ 600 ºC, as is evidenced in Figure 2b by slope close to zero observed for the

profile representing $FWHM_{OH}$ against the calcination temperature. Moreover, the regime

obtained for calcination temperatures ≤ 600 ºC exhibits a poor linear fitting, which has been

attributed to the fact that only the OH⁻ groups close to the generated reversal points can adopt

favorable orientations. Figure 2c indicates that such small changes in the orientation of the

OH⁻ groups result in a constant increment of the crystallinity, as is shown by the linear reduction of FWHM up to 600 °C. A higher energetic threshold, which is defined by the specie involved (*i.e.* OH⁻ or PO_4^{3-}), is required for further lattice refinements. This dependence on the specie is reflected by the fact that the FWHM threshold is 100 °C higher than the $FWHM_{OH}$ one. Hence, we propose a two-step mechanism regarding the HAp crystal refinement in terms of generation of vacancies and crystallinity enhancement: 1) favored OH⁻ emission up to 600 °C, which is a fast and energetically favored process due to the abundance of such species; and 2) forced OH⁻ emission at temperatures higher than 600 °C, which requires energy to overcome steric forces. The change in the trend observed for the OH⁻ species at 1100 °C anticipates the thermal decomposition of HAp into other calcium phosphate salts. This is no longer related to the crystal refinement process under study. A theoretical model for the forced emission step, which assumes equilibrium between the amount of generated of vacancies (Γ) and the water vapor pressure (P_{H2O}) is proposed, following the expressions early stated by Anderson *et al.*[25] and later used by Fujimori *et al.*:
[11]

$$2\,OH^- \leftrightarrows O^{2-}(s) + \Gamma\,(s) + H_2O\,(g) \tag{1}$$
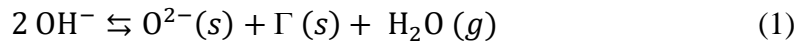
Thus, the equilibrium constant at a temperature T is defined as:

$$K(T) = \frac{[O^{2-}][\Gamma]P_{H_2O}}{[OH^-]^2} = \frac{\Gamma^2 P_{H_2O}}{(2 - 2\Gamma)^2} \tag{2}$$

$$K(T) = \exp\left(\frac{\Delta S^0}{R}\right)\exp\left(-\frac{\Delta H^0}{RT}\right) \tag{3}$$

where ΔS^0 and ΔH^0 are the standard entropy and enthalpy, respectively, and R is the gas constant. Although this model contemplates the existence of a threshold temperature (Eq. 3), it considers that: 1) the reaction is fully reversible, 2) 100% of vacancies can be generated, 3) I_{OH} is only affected by the number of vacancies, and 4) the water vapor pressure does not depend on the temperature;[11] which are in contradiction with the results presented here and

7

found in the literature.[9] In order to overcome this limitation, minor modifications have been made as follows:

$$\Gamma' \equiv \beta\Gamma \tag{4}$$

$$A_{OH}, FWHM, FWHM_{OH} \propto 1 - \Gamma' \tag{5}$$

$$I_{OH} \propto \beta + \Gamma' \tag{6}$$

where β corresponds to the maximum fraction number of vacancies that the HAp lattice can support without losing its structural integrity, which has been measured to be 50% per mol (β= 0.5).[26] The rest of parameters used, including P_{H2O} that has been assumed to behave as an ideal gas, can be found in the Supporting Information.
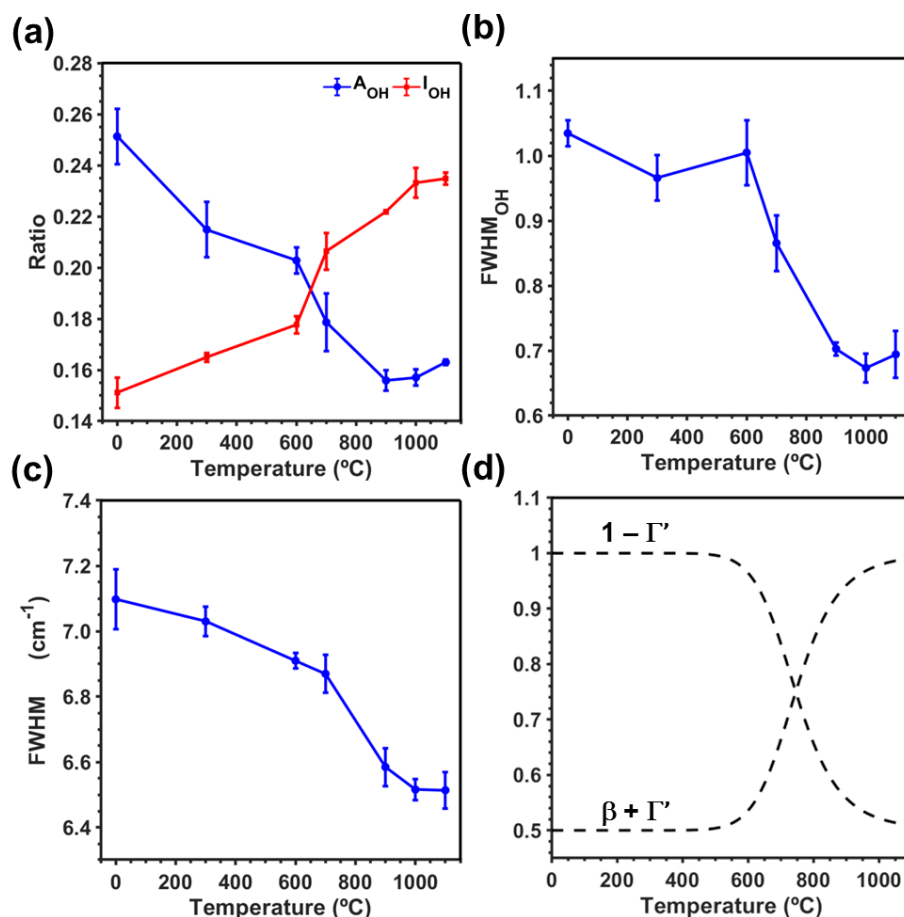

Figure 2. Study of the vacancies generation and the crystallinity as a function of the calcination temperature: (a) A_{OH} and I_{OH} ratio; (b) $FWHM_{OH}$ ratio; and (c) FWHM related to the general crystallinity of the HAp crystal lattice. (d) Results derived from the theoretical model proposed for the forced OH⁻ emission. The threshold temperature is predicted to be at ~600 °C. The error bars correspond to the standard deviations of three independent experiments.

Results depicted in Figure 2d, which represent the variation of 1–Γ' and β+Γ' against the calcination temperature, are in good accordance with the experimental measurements obtained for the forced emission, reflecting similarities in regards of the threshold temperature of 600 ºC. The theoretical model predicts that the contribution of the forced OH^- emission before the temperature threshold can be considered as negligible and, therefore, the two steps of the proposed mechanism can be well differentiated. In addition, the effect of the duration of calcination treatment at 1000 ºC was analyzed using different calcination times (*i.e.* 30 min, 1 h, 3 h and 5 h). Results clearly indicated that both crystallinity and generation of vacancies are not related to the lapse of time under treatment (Figure S6 and Table S2).

Generation of vacancies creates an electrical imbalance of species, which should be reflected by an enhancement of the superficial charge of the HAp crystals. The evolution of the surface charge, as a function of the calcination temperature, was determined by means of ζ-potential measurements. **Figure 3a** represents the variation of the ζ-potential measured at pH=7, showing the unequivocal effect of crystal refinement. Although at 600 – 700 ºC the ζ-potential presents the characteristic discontinuity found in the Raman spectra, the fact that the maximum difference in the ζ-potential (Δξ = –20 mV) is reached at 1000 ºC confirms that both A_{OH} and FWHM contribute to the superficial charge accumulation. Nonetheless, the variation of the ζ-potential against the number of vacancies, expressed as the A_{OH} ratio, is displayed in Figure 3b. Despite the relatively low accuracy of ζ-potential measurements and the fact that at high temperatures the crystallinity plays a significant role, an outstanding linear behavior is observed. On the other hand, Figure 3c depicts the variation of ζ-potential measurements for HAp-25, and HAp-1000 against the pH, while Figure S7 provides the results for samples calcined at 300, 600, 700 and 1100 ºC. As is shown, the crystal lattice refinement causes significant changes in the accumulation of negative surface charge for a

wide range of pH, reflecting that vacancies favor the dominance of negatively charged species

over Ca^{2+} ions at the surface.
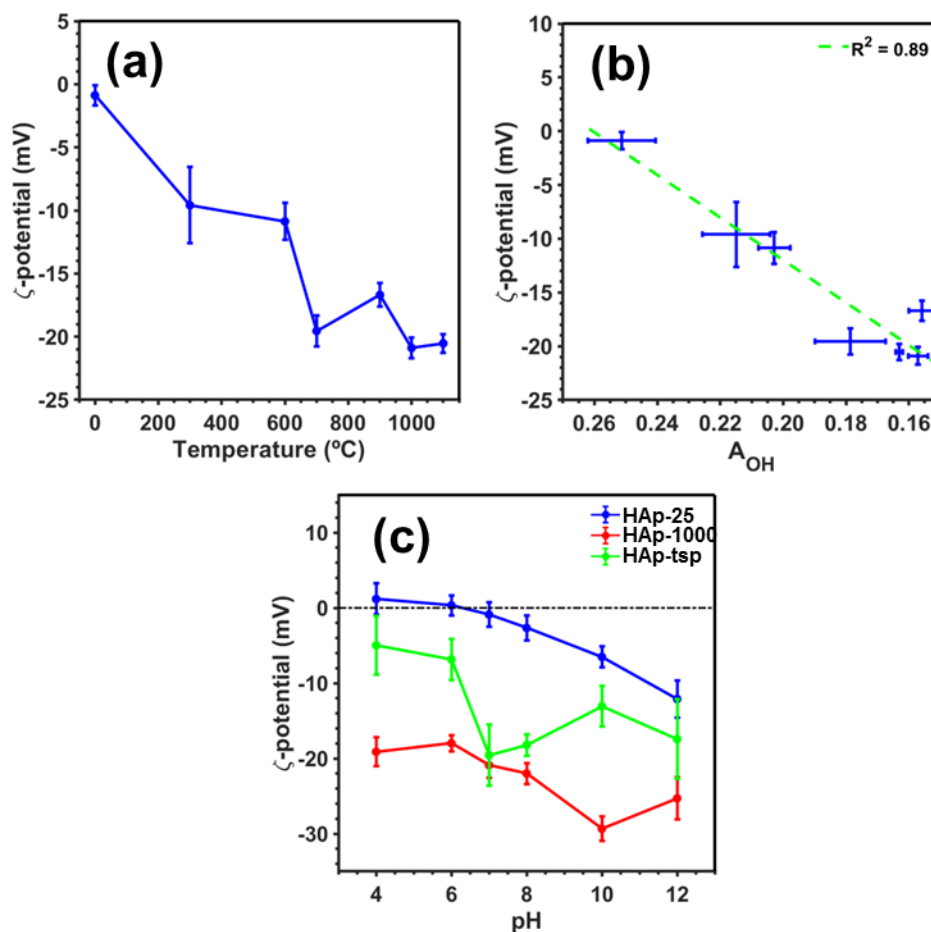
Figure 3. (a) Evolution of the ζ-potential at pH = 7 as a function of the calcination temperature. (b) Variation of the ζ-potential against the generation of vacancies (A_{OH}). The linear fitting is highlighted in green dotted line. (c) Variation of the ζ-potential versus pH in the 4 – 12 interval for HAp-25, HAp-1000 and HAp-tsp samples. The error bars correspond to the standard deviations of three independent experiments.

As a proof of concept, the ζ-potential of the sample obtained by applying the TSP process (*i.e.*

compressing powdered HAp-1000 into pellets and exposing them to a 500 V at 1000 °C for 1

h), hereafter denoted as HAp-tsp, were also measured. Amazingly, the results plotted in

Figure 3c do not show the expected substantial enhancement of the surface charge with

respect to the HAp-1000 sample. Indeed, the ζ-potential of HAp-tsp is less negative than that

of HAp-1000. This observation is apparently contradictory with the experimental results

reported up to the date[15,16] since extra charge accumulation in the crystal boundaries is not

detected.[10] Therefore, in depth revision of the polarization mechanisms arising from the electrical enhanced properties by direct measurements and careful characterization is mandatory. Moreover, the fact that the ζ-potential values at pH = 7 are very similar for both samples (-20.9 and -19.6 mV for HAp-1000 and HAp-tsp, respectively) indicates that no extra vacancies have been generated during the TSP process. This point is carefully assessed in the next section.

2.2. TSP Treatment: Vibrational Studies

Raman microscopy relies on the differential polarizability of bonds, which is induced by the vector electric field of the incident beam:

$$\vec{\mu} = [\alpha]\vec{E} \tag{7}$$

where $\vec{\mu}$, $\vec{E}$ and $[\alpha]$ represent the dipole moment of the molecule, the electric vector of the incident light and the polarizability tensor, respectively. This technique has allowed the use of polarized light for the successful study of the molecular orientation in polymers[27] and graphene.[28] The polarizability tensor must be understood as an unique volume surrounding and correspondingly aligned with each bond, which is going to weight (when expressed in the same coordinates through Euler angles) the contributions of the incident light on the final dipole moment. Thus, proper selection of the polarization of the incident beam allows controlling the scattered intensity of each molecule. In this work, a similar approach with unpolarized light has been considered, due to equipment requirements, assuming that: 1) HAp-1000 presents OH$^-$ groups pointing to unspecific directions; 2) the weight contribution of the polarizability tensors will be maximal when the incident light is unpolarized; 3) for HAp-tsp samples, part of the OH$^-$ groups are pointing towards a specific direction; and 4) the final induced dipole moment will be lowered because of the corresponding projections of the weights of $[\alpha]$. Hence, the final I_{OH} is expected to decrease with increasing amount of OH$^-$

groups pointing towards a specific direction (fundamentals are described in the Supporting Information). These assumptions have been schematically depicted in **Scheme 1**.
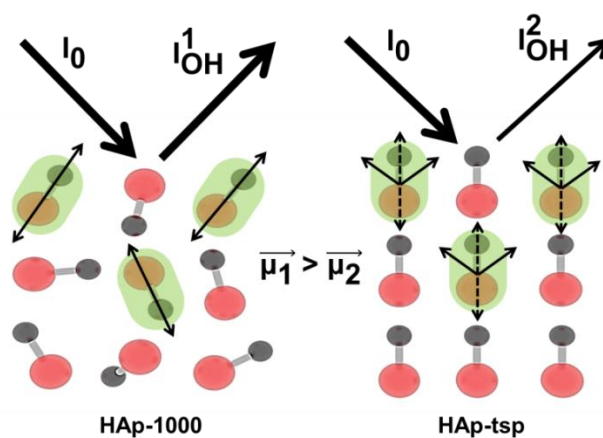
Scheme 1. Approach used for the direct measurement of the reorientation of OH⁻ groups using unpolarized light. Green clouds simulate the Raman tensors.

Figure 4 presents the complete analysis of the Raman spectra recorded for HAp-1000 and HAp-tsp samples. As expected, a considerable difference is observed in the I_{OH} due to the specific orientation of the OH⁻ exerted by the TSP treatment, presenting for the first time a direct evidence of such orientation. Accordingly, the crystallinity did not show any substantial change and the lower value of A_{OH} was not attributed to the generation of new vacancies (also shown by the ζ-potential results) but to the lowering of the measured intensity (*i.e.* time of exposure at 1000 °C did not affect the crystal lattice of HAp, as demonstrated in Figure S5). It is worth noting that the analysis of all samples was performed using the same pellet (*i.e.* prepared with the same compressed HAp-1000 powder) to ensure good comparison. Then, the pellet was 1) trenched and compressed again (HAp-tsp-T), and 2) sintered at 1000 °C for 2 h (HAp-tsp-TS). Comparison of the spectroscopic results obtained for HAp-tsp, HAp-tsp-T and HAp-tsp-TS, which are included in Figure 4, indicates how I_{OH} increases from 0.15 for HAp-tsp to 0.20 and 0.21 for HAp-tsp-T and HAp-tsp-TS respectively, without reaching the 0.22 of HAp-1000. This was attributed to the fact that despite of conserving the specific dipole orientation at the crystal grain level, the general micro specific orientation was lost.

12

It is worth noticing how this recovery supports the fact that the observed variations in I_{OH} and A_{OH} are due to the orientation of the dipoles since restoration of vacancies is not possible at 1000 ºC. These results not only allow the definition of an effective yield of polarization by means of a fast and low cost technique but also, and in combination with the ζ-potential measurements, suggests that the enhanced electrical properties reported in the literature are due to bulky aspects rather than local crystallographic space charge accumulation. This feature opens a new perspective in regards of the mechanism proposed by Yamashita and co-workers,[10] indicating that the polarization of early formed HAp particles in the micrometric or submicrometric range is preferred in order to enhance the effect of the polarization.
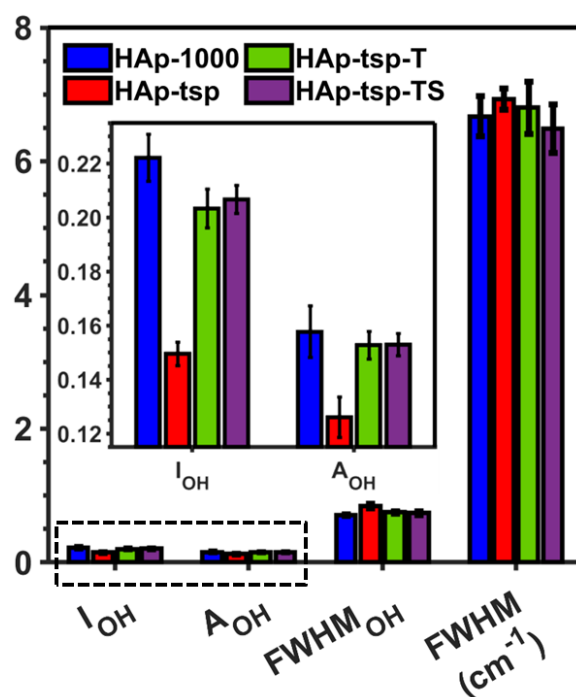

Figure 4. Comparison of the parameters derived by Raman spectroscopy (A_{OH}, I_{OH}, $FWHM_{OH}$ and FWHM) for HAp-1000, HAp-tsp, HAp-tsp-T and HAp-tsp-TS samples. The error bars correspond to the standard deviations of three independent experiments.

2.3. Electrical Characterization

Precise measurements in the micrometric / nanometric scale lengths are desirable to prove the conclusions reached in previous sections. Indeed, a crucial point is to determine whether charge accumulation is achieved through the TSP treatment and at what level. Although AFM is normally used for characterizing the sample topography, the metallic nature of the

cantilever is expected to detect variations in its tapping regime due to electrostatic forces caused by the charge accumulation on the surface. Initially, a topographic characterization of the samples was performed, the 3D reconstructed surface images of HAp-1000 and HAp-tsp pellets are depicted in **Figure 5a-b**. HAp-1000 pellets are formed by grains in the size range of 100-300 nm, which tend to agglomerate forming particles up to 1 μm. For HAp-tsp pellets, the effect of sintering on these particles is clearly observed, which is attributed to the fact that, during the TSP treatment, the pellet has been exposed at 1000 °C. Thus, the root-mean-square roughness (R_q) of HAp-tsp ($R_q = 46.2 \pm 9.4$ nm) is considerably lower than that of the former ($R_q = 367 \pm 82$ nm).
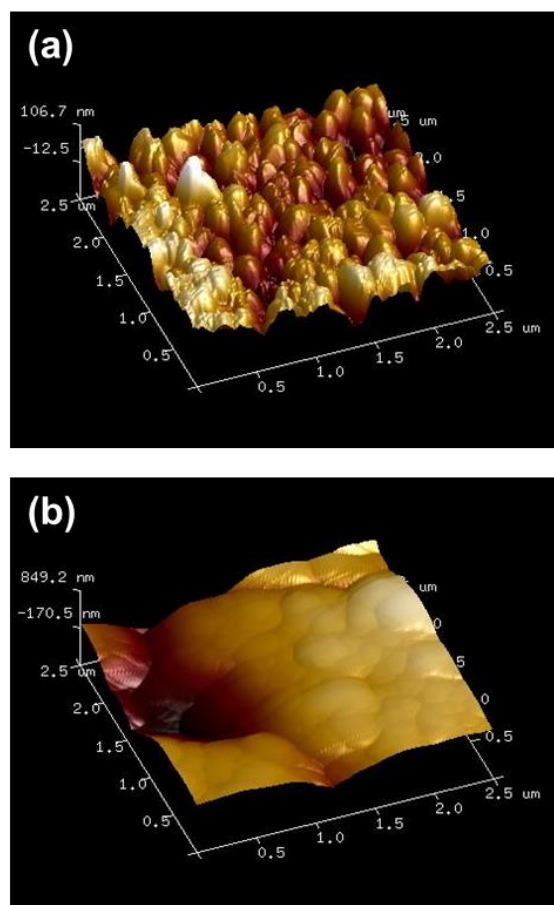

Figure 5. 3D topographic AFM image (2.5×2.5 μm^2) of (a) HAp-1000 and (b) HAp-tsp pellets.

In order to ascertain if the results of the TSP treatment could be reproduced without applying the electric voltage, a HAp-1000 pellet was sintered for 2 h at 1000 °C, the resulting sample

14

being denoted as HAp-1000-S. With the intention of characterizing the appearance of space charge accumulation, amplitude images of the electric signal controlling the cantilever for HAp-1000, HAp-1000-S and HAp-tsp were compared. **Figure 6a** displays a representative 5×5 μm^2 amplitude image for HAp-tsp, while images for HAp-1000 and HAp-1000-S are shown in Figure S8. HAp-tsp exhibits pronounced electrostatic distortions, which are mainly located at the boundaries among the microscopic grains, this effect being much more attenuated for HAp-1000 and HAp-1000-S. Cross section data, which are presented in Figure 6b for the three samples, allows to distinguish the characteristic distortion in form of high-frequency vibration on the cantilever due to the charge accumulation in HAp-tsp. The fact that this kind of vibration does not appear continuously along the cross section, together with the presence of perpendicular ones, discards the existence of artifacts caused by the cantilever during the measurement.

These results indicate that the TSP treatment generates surface charge accumulation at the micrometric grain boundaries rather than in the crystal domains. Such accumulation is spontaneously created by the generation of vacancies, as proved by ζ-potential measurements. It is important to highlight how imposing a specific orientation in all the crystal domains allows the delocalization of the charges along the whole crystal, drastically increasing its surface charge. Hence, the bigger the microscopic grain, the higher the contribution of charges to the boundary. This effect can be observed in the magnified image included in Figures 6a and its corresponding cross section (Figure 6c). These results provide understanding to the ζ-potential results displayed in Figure 3c, which showed that the average value of HAp-1000 is more negative than that of HAp-tsp one.
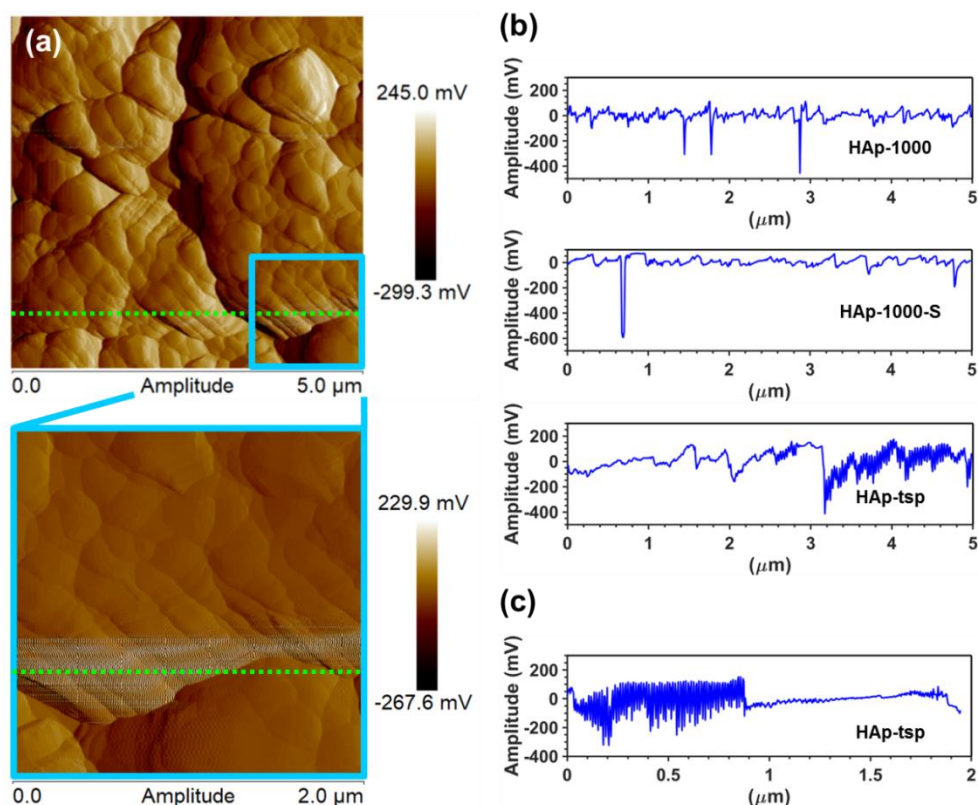
Figure 6. (a) 2D amplitude AFM images (5×5 and 2×2 μm^2) of HAp-tsp used to characterize the space charge accumulation by following the amplitude of the voltage applied in the cantilever. (b) Representative cross section data obtained for HAp-1000, HAp-1000-S and HAp-tsp, which have been taken from the 5×5 μm^2 amplitude images Figures S8 and 6a. (c) Cross section data obtained for HAp-tsp using the 2×2 μm^2 amplitude image displayed in (a).

The sintering process restricts the charges at the crystalline domains, disfavoring charge accumulation in the grain boundaries. In order to elucidate the importance of this contribution with respect to the ordering of the OH⁻ groups, AFM measurements were performed on HAp-1000-S and HAp-tsp-T samples considering smaller windows. Representative images displayed in **Figure 7a-b** indicate that charge accumulation is again observed in the grain boundaries for both samples. Although sintering seems to play a major contribution (HAp-1000-S shows higher charge accumulation), it has to be taken into account that the huge difference in grain sizes reduces considerably the maximum number of charges available in the HAp-tsp-T grains (Figure 7c). Overall, it can be stated that imposing a specific orientation results in favoring the quantum electric pathways through the different crystalline domains,

16

while sintering increases the number of available charges generated by the presence of OH⁻ vacancies in the crystal lattice (*i.e.* due to the bigger size of the crystalline domains). In any case, the synergy between both effects produces unequivocally a much higher electrical enhancement for HAp-tsp pellet, which is in full agreement with the experimental measurements presented here.
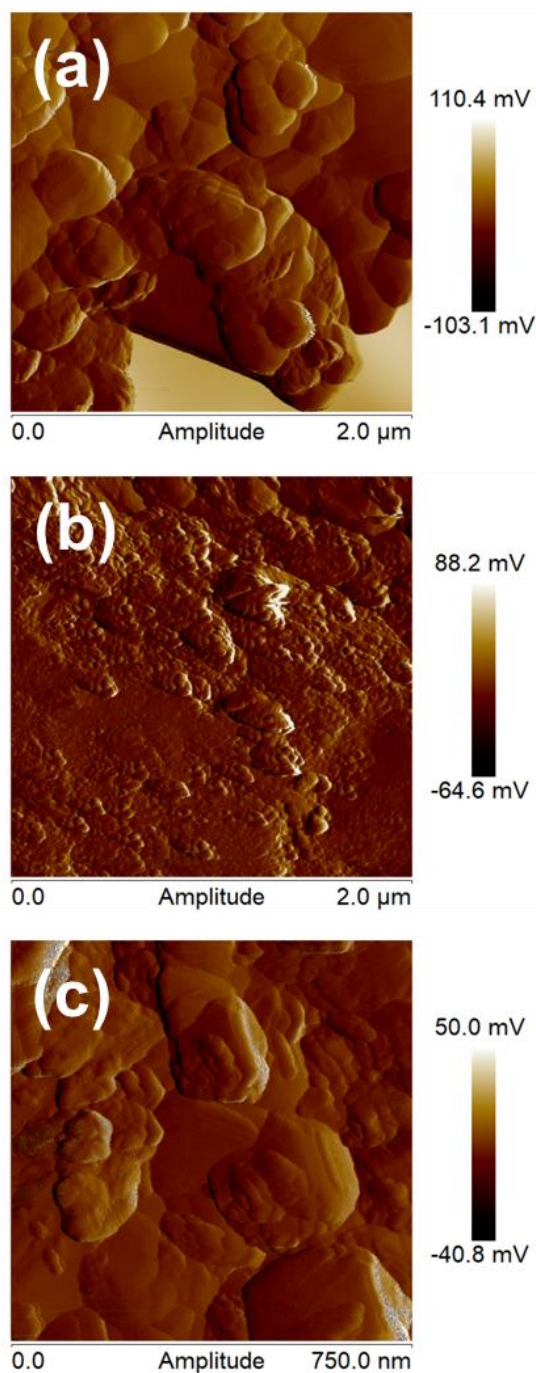

Figure 7. 2D amplitude AFM images of (a) HAp-1000-S (2×2 µm²), (b) HAp-tsp-T (2×2 µm²) and (c) HAp-tsp-T (750×750 nm²) pellets.

All in all, in this work we provide direct experimental evidences about the fact that the charge accumulation associated to the TSP treatment does not occur in the crystalline domains. This observation is in opposition with previously hypothesized mechanisms.[10,15] More specifically, our results demonstrate that the TSP treatment allows the delocalization of the charges generated by the induced OH^- vacancies, which move across different crystalline domain and accumulate in the crystal boundaries. Although the generation of vacancies and the increase of crystallinity affect the electrical properties of HAp at the crystal lattice level, the TSP is mainly associated to the bulk of the micrometric particles. Indeed, together with the intrinsic sintering of the TSP treatment, we prove that the polarization of samples with pre-formed HAp micrometric particles is preferred for producing HAp with enhanced electrical properties.

2.4. Implications of the TSP in the Catalytic Activity

The utilization of HAp-based catalysts for the electro-photo-synthesis of glycine (Gly) and alanine (Ala) amino acids by carbon and nitrogen fixation from CH_4, CO_2 and N_2 under mild reaction conditions has been reported recently.[7,29] In the present study, we show that the catalytic activation of this reaction is strongly dependent on the electrical enhancement of HAp achieved by the TSP treatment. More specifically, Gly and Ala were produced using a reactor with an inert reaction chamber (120 mL), in which the catalyst (~150 mg) and water (0.5 mL) were incorporated, and a UV lamp (253.7 nm) protected by a UV transparent quartz tube to irradiate the catalyst. Reactions were performed at an initial pressure of 6 bar, which was reached by introducing sequentially 2 bar of each feeding reaction gas (*i.e.* N_2, CO_2 and CH_4), and at 95 ºC. The reaction time was 48 h in all cases and the reaction products were analyzed by ^1H NMR spectroscopy. All experimental details are provided in the Supporting Information.

In this work, HAp-tsp or HAp-tsp-T, which were coated with zirconyl chloride and aminotris(methylenephosphonic acid) using a previously described process (see Supporting Information),[29] were used as catalysts. The efficiency of such two catalysts, which was analyzed in terms of Gly and Ala yield, is compared in **Figure 8**. As it can be seen, the yield of amino acids decreased one order of magnitude when the HAp-tsp catalyst was replaced by the HAp-tsp-T one. More specifically, the yield of Ala and Gly was ~85% lower for HAp-tst-T than for HAp-tsp. This fact clearly indicates that the charge accumulation plays a crucial role in the reaction, supporting the mechanism proposed in this work. Additionally, this result stresses the importance of controlling the micrometric geometry of the HAp-based catalysts before, rather than after, the TSP treatment. Hence, the utilization of powdered structures (mainly used for continuous reactions) is expected to diminish the yield of the reaction (as seen for HAp-tsp-T) despite of the increase of the exposed surface.
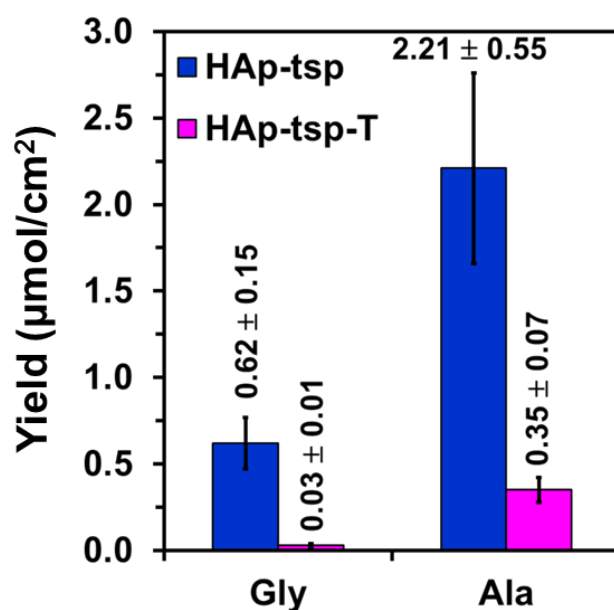
Figure 8. Yield of Ala and Gly, expressed in μmol of product per area of the catalyst (cm^2), for the reactions performed with HAp-tsp and HAp-tsp-T catalysts. The error bars correspond to the standard deviations of three independent experiments.

3. Conclusion

Raman microscopy has been shown to be a useful and efficient technique for the precise characterization of the OH⁻ groups after both calcination and TSP treatments. The combination of Raman microscopy and AFM, as a novel approach, allows us to state that the enhanced electrical properties of HAp crystals arise from two different and distinguishable phenomena: 1) the generation of vacancies inside the HAp lattice, which is responsible of creating available charges, due to the calcination treatment; and 2) the specific orientation of the ions in the OH⁻ columns (TSP treatment) that allows the delocalization of charges along all the independent crystalline domains of the HAp particles, and as a consequence, reinforcing the charge accumulation at the micrometric scale, particularly at grain boundaries. Although most of the fundamentals proposed in the literature have been for the first time experimentally corroborated, the discrimination between crystal lattice (calcination) and bulk effects (TSP) has been introduced. Therefore, for the calcination treatment, the amount of generated vacancies significantly increases after 600 ºC, the optimal value being reached at 1000 ºC. Moreover, the size and ordering of grain particles favoring the initial sintering process are important for the posterior TSP treatment. Moreover, the proposed model has demonstrated to have a direct impact in the catalytic properties of HAp-tsp, corroborating that charge accumulation is mainly located at the boundaries among the microscopic grains. The unprecedented possibility of relating the presence and orientation of OH⁻ groups with the final electrical properties of HAp by means of Raman microscopy and AFM techniques not only paves the way for further optimization of polarized ceramics, but also provides a powerful tool for the design and characterization of the next generation of electrically tuned calcium phosphate minerals.

4. Experimental Methods

Synthesis of HAp. Highly crystalline HAp has been obtained following a hydrothermal synthesis route, using $(NH_4)_2HPO_4$ and $Ca(NO_3)_2$ as starting reagents. After washing, the

20

resulting HAp was frozen and dried by means of lyophilization for 3 days. A white HAp powder was obtained. Complete description of the synthetic route is described in the Supporting Information.

Calcination and TSP processes. The calcination treatment was performed using a Carbolite ELF11/6B/301 furnace, where the synthesized HAp powder was exposed for 2 h to the desired temperature. The following calcination temperatures were considered in this work: 300, 600, 700, 900, 1000 and 1100 ºC. The TSP process was achieved by compressing powdered samples calcined at 1000 ºC into pellets and, subsequently, exposing them to a 500 V at 1000 ºC for 1 h. Samples were allowed to cool down maintaining the voltage for 30 min. Other configurations regarding trenching or re-sintering of the samples are explicitly explained. All measurements on calcined and TSP samples were conducted at room temperature.

Characterization of the samples. InVia Qontor confocal Raman microscope (Renishaw), equipped with a Renishaw Centrus 2957T2 detector was used for structural characterization of HAp. A 532 nm laser (unless specified) was selected, measuring the average of 4×4 grids for each sample in order to ensure obtaining representative data. Zeta (ζ)-potential measurements were carried out in a NanoBrook 90Plus Zeta equipped with an AQ-1321. Finally, atomic force microscopy (AFM) images were acquired with a Molecular Imaging PicoSPM and a NanoScopIV controller, under ambient conditions. Specific details are provided in the Supporting Information.

Supporting Information

Supporting Information is available from the Wiley Online Library or from the author.

Acknowledgements

![WILEY-VCH]

References

[1]   a) H. Li, D.B. Wu, J. Wu, L. Y. Dong, Y. J. Zhu, X. L.Hu, *Adv. Mater.* **2017**, *29*, 1703548; b) M. Nakayama, S. Kajiyama, A. Kumamoto,T. Nishimura, Y. Ikuhara, M. Yamato, T. Kato, *Natur. Commun.* **2018**, *9*, 568; c) M. Harja, G. Ciobanu, *Sci. Total Environ.* **2018**, *628-629*, 36; d) M. T. Hua, J. L. Song, C. Xie, H. R. Wu, Y. Hu, X. Huang, B. X. Han, *Green Chem.* **2019**, *21*, 5073; e) S. Wasthi, S.K. Pandey, E. Arunan, C. Srivastava, *J. Mater. Chem. B* **2021**, *9*, 228.

[2]   a) G. Popescu-Pelin, C. Ristoscu, L. Duta, G. E. Stan, I. Pasuk, T. Tite, M. S. Stan, C. Bletou, M. Popa, M. C. Chifiriuc, F. N. Oktar, A. Nicarel, N. Mihalescu, *ACS Sust. Chem. Eng.* **2020**, *8*, 4026; b) T. S. Phan, A. R. Sane, B. Rêgo de Vasconcelos, A. Nzihou, P. Sharrock, D. Grouset, D. Pham Minh, *Appl. Catal. B Environ.* **2018**, *224*, 310; c) M. Frasnelli, F. Cristofaro, V. M. Sglavo, S. Dirè, E. Callone, R. Ceccato, G. Bruni, A.I. Cornaglia, L. Visai, *Mater. Sci. Eng. C*, **2017**, *71*, 653; d) L. Yu, D. W. Rowe, I.P. Perera, J.Y. Zhang, S.L. Suib, X. N. Xin, M. Win, *ACS Appl. Mater. Interfaces* **2020**, *12*, 18235; e) Y. Q. Tang, Q. Y. Wang, Q. F. Ke, C. Q. Zhang, J. J. Guan, Y. P. Guo, *Chem. Eng. J.* **2020**, *387*, 124166; f) Y. Liu, Y.X. Tang, J. Wu, J. Sun, X. Liao, Z.G. Teng, G.M. Lu, *J. Colloid Interface Sci.* **2020**, *570*, 402; g) K.W. Jung, S.Y. Lee, J.W. Choi, Y.J. Lee, *Chem. Eng. J.* **2019**, *369*, 529.

[3] a) A. Joseph Nathanael, D. Mangalaraj, N. Ponpandian, *Compos. Sci. Technol.* **2010**, *70*, 1645; b) A. Joseph Nathanael, S.I. Hong, D. Mangalaraj, N. Ponpandian, P. C. Chen, *ryst. Growth Des.* **2012**, *12*, 3565; c) A. Joseph Nathanael, D. Mangalaraj, P. Chi Chen, N. Ponpandian *J. Nanopart. Res.* **2011,** *13,* 1841.

[4]   a) H. D. Kim, H. L. Jang, H. Y. Ahn, H. K. Lee, J. Park, E. S. Lee, E. A. Lee, Y. H. Jeong, D. G. Kim, K. T. Nam, N. S. Hwang, *Biomaterials* **2017**, *112*, 31; b) P. Yu, R. Y. Bao, X. J. Shi, W. Yang, M.B. Yang, *Carbohydr. Polym.* **2017**, *155*, 507; c) H. W. Tong, M. Wang, W. W. Lu, *Nanomedicine* **2013**, *8*, 577.

[5]   a) M. Nakamura, N.Hori, H. Ando, S. Namba, T. Toyama, S. Nishimiya, K. Yasmashita, *Mater. Sci. Eng. C* **2016**, *62*, 283; b) M. Rivas, L. J. Valle, A. M. Rodriguez-rivero, P. Turon, J. Puiggali, C. Alemán, J. Puiggalí, C. Alemán, *ACS Biomater. Sci. Eng.* **2018**, *4*, 3234.

[6]   S. Hu, F. Jia, C. Marinescu, F. Cimpoesu, Y. Qi, Y. Tao, A. Stroppa, W. Ren, *RSC Adv.* **2017**, *7*, 21375.

[7]   M. Rivas, L. J. del Valle, P. Turon, C. Alemán, J. Puiggalí, *Green Chem.* **2018**, *20*, 685.

[8]   G. Revilla-López, J. Sans, J. Casanovas, O. Bertran, J. Puiggalí, P. Turon, C. Alemán, *Appl. Catal. A Gen.* **2020**, *596*, 117526.

[9]   K. Yamashita, K. Kitagaki, T. Umegaki, *J. Am. Ceram. Soc.* **1995**, *78*, 1191.

[10]   N. Horiuchi, M. Nakamura, A. Nagai, K. Katayama, K. Yamashita, *J. Appl. Phys.* **2012**, *112*, 1.

[11]   H. Fujimori, H. Toya, K. Ioku, S. Goto, *Chem. Phys. Lett.* **2000**, *325*, 383.

[12]   J. Sans, J. Llorca, V. Sanz, J. Puiggalí, P. Turon, C. Alemán, *Langmuir* **2019**, *35*, 14782.

[13]   A. J. Ruys, M. Wei, C. C. Sorrell, M.R. Dickson, A. Brandwood, B. K. Milthorpe, *Biomaterials* **1995**, *16*, 409.

[14]   G. Ma, X. Y. Liu, *Cryst. Growth Des.* **2009**, *9*, 2991.

[15]   N. Horiuchi, S. Nakaguki, N. Wada, K. Nozaki, M. Nakamura, A. Nagai, K. Katayama, K. Yamashita, *J. Appl. Phys.* **2014**, *116*, 014902.

[16] M. Rivas, L. J. delValle, E. Armelin, O. Bertran, P. Turon, J. Puiggalí, C. Alemán, *ChemPhysChem* **2018**, *19*, 1746.

[17] C. Fu, K. Savino, P Gabrys, A. Zeng, B. Guan, D. Olvera, C. Wang, B. Song, H. Awad, Y. Gao, M. Z. Yates, *Chem Mater.* **2015**, *27*, 1164.

[18] S. Nakamura, H. Takeda, K. Yamashita, *J. Appl. Phys.* **2021**, *89*, 5386.

[19] S. A. M. Tofail, D. Haverty, K. T. Stanton, J. B. McMonagle, *Ferroelectrics* **2005**, *319*, 117.

[20] N. Horiuchi, N. Wada, K. Nozaki, M. Nakamura, A. Nagai, K. Yamashita, *J. Appl. Phys.* **2016**, *119*, 1.

[21] a) Z. Iqbal, V. P. Tomaselli, O. Fahrenfeld, K. D. Möller, F. A. Ruszala, E. Kostiner, *J. Phys. Chem. Solids* **1977**, *38*, 923–927; b) V. Devarajan, W. E. Klee, *Phys. Chem. Minerals* **1981**, *7*, 35.

[22] S. Koutsopoulos, *J. Biomed. Mater. Res.* **2002**, *62*, 600.

[23] P. N. De Aza, F. Guitián, C. Santos, S. De Aza, R. Cuscó, L. Artús, *Chem. Mater.* **1997**, *9*, 916.

[24] J. C. Elliott, P. E. Mackie, R. A. Young, *Science* **1973**, *180*, 1055.

[25] J. S. Anderson, M. W. Roberts, F. S. Stone, Reactivity of solids: Proceedings of the seventh international symposium on the reactivity of solids, Bristol, 17-21 July 1972. Chapman and Hall: London , **1972**, pp xvii, 812 p.

[26] H. Owada, K. Yamashita, T. Umegaki, T. Kanazawa, *J. Ceram. Soc. Japan* **1989**, *97*, 1087.

[27] M. Tanaka, R. J. Young, *J. Mater. Sci.* **2006**, *41*, 963.

[28] S. Sahoo, R. Palai, R. S. Katiyar, *J. Appl. Phys.* **2011**, *110*, 44320.

[29] J. Sans, E. Armelin, V. Sanz, J. Puiggalí, P. Turon, C. Alemán, *J. Catal.* **2020**, *389*, 646.

Both the generation of OH⁻ vacancies at high temperatures and the OH⁻ orientations imposed through the polarization treatment at the surface of permanently polarized hydroxyapatite electrocatalysts have been monitored combining spectroscopy and microscopy measurements. The implications of such superficial changes on the catalytic activity have been evaluated using a reaction to yield amino acids from a mixture of gases.

J. Sans,* M. Arnau, F. Estrany, P. Turon,* C. Alemán*

Regulating the Superficial Vacancies and OH⁻ Orientations on Polarized Hydroxyapatite Electrocatalysts
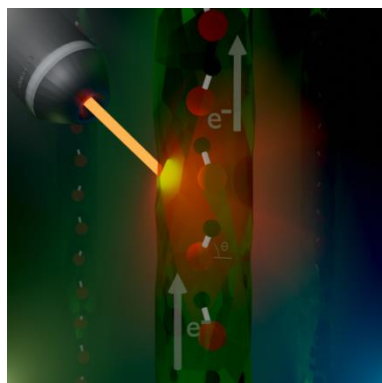
Supporting Information

Regulating the Superficial Vacancies and OH⁻ Orientations on Polarized Hydroxyapatite Electrocatalysts

Jordi Sans, Marc Arnau, Francesc Estrany, Pau Turon* and Carlos Alemán**

EXPERIMENTAL METHODS

Materials

Calcium nitrate $Ca(NO_3)_2$, diammomium hydrogen phosphate [$(NH_4)_2HPO_4$; purity > 99.0%], ammonium hydroxide solution 30% [NH_4OH; purity: 28-30% w/w], zirconyl chloride ($ZrOCl_2 \cdot 8H_2O$), aminotris(methylenephosphonic acid) (ATMP) and were purchased from Sigma Aldrich. Ethanol (purity > 99.5%) was purchased from Scharlab. N_2, CH_4 and CO_2 gases with a purity of > 99.995% were purchased from Messer. All experiments were performed with milli–Q water.

Synthesis hydroxyapatite (HAp)

15 mL of 0.5 M of $(NH_4)_2HPO_4$ in de-ionized water were added at a rate of 2 mL/min to 25 mL of 0.5 M of $Ca(NO_3)_2$ in ethanol (with pH previously adjusted to 11 using ammonium hydroxide solution) and left aging for 1 h. The whole process was performed under gentle agitation (150 rpm) and at room temperature. Hydrothermal treatment at 150 ºC was applied using an autoclave Digestec DAB – 2 for 24 h. The autoclave was allowed to cool down before opening. The precipitates were separated by centrifugation and washed with water and a 60/40 v/v mixture of ethanol – water (twice). After freeze – drying it for 3 days, a white powder was obtained. The concentrations of $(NH_4)_2HPO_4$ and $Ca(NO_3)_2$ solutions, which were identical in all cases, and the pH were varied to regulate the crystallinity and stoichiometry of HAp. Table S1 lists the conditions used for preparation of each sample.

Characterization methods

Vibrational studies were completed using FTIR spectroscopy. Spectra were recorded on a

FTIR Jasco 4100 spectrophotometer through an attenuated total reflection accessory (Top-

plate) with a diamond crystal (Specac model MKII Golden Gate Heated Single Reflection

Diamond ATR). Samples were evaluated using spectra manager software and, for each

sample 64 scans were performed between 4000 and 600 cm^{-1} with a resolution of 4 cm^{-1}.

Wide angle X-ray scattering (WAXS) studies were conducted using a Brucker D8 Advance

model with Bragg-Brentano 2θ configuration and Cu K$_\alpha$ radiation ($\lambda = 0.1542$ nm).

Measurements were performed in a 2θ range of 20º –60º in steps of 0.02º, and a scan speed of

2 s using a one-dimensional Lynx Eye detector. The crystallinity (χ_c) was obtained using the

following expression:

$$\chi_c = 1 - \frac{V_{112/300}}{I_{300}} \tag{S1}$$

where I_{300} is the intensity of the (300) reflection and $V_{112/300}$ is the intensity of the hollow

between the (112) and (300) reflections, which disappears in non-crystalline samples.

Zeta (ζ)-potential measurements were performed suspending 1.5 mg of HAp in 5 mL of a 1

mM KCl water solution, previously sonicated for 3 minutes. The pH of the solution was

controlled with H_2SO_4 and NaOH using a Crison pH meter GLP – 21.

Atomic force microscopy (AFM) studies were conducted to obtain topographic images of the

surface of samples using silicon TAP 150-G probes (Budget Sensors, Bulgaria) with a

frequency of 150 kHz and a constant force of 5 N/m. Images were obtained with an AFM

Dimension microscope using the NanoScope IV controller under ambient conditions in

tapping mode. The row scanning frequency was set of 1Hz. The root mean square roughness

(Rq), which is the average height deviation taken from the mean data plane, was determined

using the statistical application of the NanoScope Analysis software (1.20, Veeco). In the

amplitude channel of the scanned window, disturbances due to charge accumulation at the

grain boundaries were clearly detected. Sectional images of the cantilever vibration distortion zones due to the accumulation of charge on the scanned surface were obtained with the "slice" option of the Nanoscope Analysis Software (1.20, Veeco).

Preparation of HAp-based catalysts

ATMP, zirconyl chloride and ATMP coatings were prepared by depositing some drops of the corresponding solutions, which were 50, 10 and 50 mM respectively, onto HAp-tsp and HAp-tsp-T. After deposition of each coating layer, samples were dried at room temperature for at least 12 hours before deposition of the next layer.

Synthesis of Amino Acids

A high pressure stainless steel reactor bearing an inert reaction chamber coated with a perfluorinated polymer (120 mL) was used for the synthesis of amino acids.[S1] The reactor was equipped with an inlet valve for the entrance of N_2, CH_4, CO_2 and an outlet valve to recover the gaseous reaction products. A UV lamp (GPH265T5L/4, 253.7 nm) was also placed in the middle of the reactor to irradiate the catalyst directly, the lamp being protected by a UV transparent quartz tube. The catalysts (150 mg) and deionized liquid water (0.5 mL) were initially introduced into the reaction chamber.

The reactions were performed at 95 °C using a reaction time of 48 h. The chamber was extensively purged with the first selected gas in order to eliminate the initial air content. Each selected gas was introduced to increase the reaction chamber pressure (measured at room temperature) to the target pressure. In all cases the chamber pressure was increased up to 6 bar by introducing sequentially 2 bar of each feeding reaction gas (*i.e.* N_2, CH_4, CO_2).

The reaction products were analyzed by ^1H NMR spectroscopy. All ^1H NMR spectra were acquired with a Bruker Avance III-400 spectrometer operating at 400.1 MHz. The chemical shift was calibrated using tetramethylsilane as internal standard. Sixty-four scans were

recorded in all cases. In order to remove the amino acids from the catalyst, samples were dissolved in deuterated water containing 100 mM of HCl and 50 mM of NaCl with the final addition of deuterated water.

THEORETICAL ASSUMPTIONS

Forced OH⁻ emission model

It has been assumed that the values of $\exp\left(\frac{\Delta S^0}{R}\right)$ and ΔH^0 in Eq. 3 are independent from temperature and correspond to $1.2 \cdot 10^9$ and 251 kJ/mol, respectively.[S2] T and R has been set to be in the proper units (K, and J/(K·mol), respectively). Accordingly, P_{H2O} has been assumed to behave as an ideal gas and, therefore, $P_1 \cdot T_1 = P_2 \cdot T_2$, because the volume is maintained. The water vapor pressure (P_{H2O}) was considered to be 0.023 atm at 23 ºC.

Raman microscopy fundamentals and assumptions

As it has been explained, when light encounters a molecule, the electric field of the light ($\vec{E}$) induce a dipole moment ($\vec{\mu}$) in the molecule due to its polarizability, which is defined as:

$$\vec{\mu} = [\alpha]\vec{E} \tag{S2}$$

where $[\alpha]$ is a tensor expression of the polarizability (polarization tensor), which is considered to be a second–rank tensor. It is wort noting that $[\alpha]$ and $\vec{E}$ should be expressed in the same coordinate system X-Y-Z, even though in general this is not accomplished since the polarization tensor is usually referred considering the origin point the coordinates and the orientation of the molecule (x'-y'-z'). Thus, proper transformation considering Euler angles must be applied as follows:

$$[\alpha]_{X-Y-Z} = R_Z(\psi)R_Y(\theta)R_X(\phi)[\alpha']_{x-y-z}$$

$$= \begin{pmatrix} cos\theta cos\psi & -cos\theta sin\psi + sin\phi sin\theta cos\psi & sin\phi sin\psi + cos\phi sin\theta cos\psi \\ cos\theta sin\psi & cos\phi cos\psi + sin\phi sin\theta sin\psi & -sin\phi cos\psi + cos\phi sin\theta sin\psi \\ -sin\theta & sin\phi cos\theta & cos\phi cos\theta \end{pmatrix} [\alpha']_{x-y-z} \tag{S3}$$

Hence the Eq. S2 can be expressed as follows:

$$\vec{\mu} = R_Z(\psi)R_Y(\theta)R_X(\phi)[\alpha']_{x-y-z}\vec{E}_{X-Y-Z} \tag{S4}$$

It has been assumed that the hydroxyl groups of the HAp lattice might adopt different

orientations ($[\alpha_{HAp}]$) and, therefore, no change of coordinate system is needed when using

unpolarized light. However, when a specific general orientation is imposed in HAp-tsp, a

different coordinate system is generated ($\left[\alpha'_{HAp-tsp}\right]_{x-y-z}$) and, thus, its projections are

needed to take into. Thus,

$$\vec{\mu}_{HAp} = [\alpha_{HAp}]_{X-Y-Z}\vec{E}_{X-Y-Z} > \vec{\mu}_{HAp-tsp}$$

$$= R_Z(\psi)R_Y(\theta)R_X(\phi)\left[\alpha'_{HAp-tsp}\right]_{x-y-z}\vec{E}_{X-Y-Z} \therefore \tag{S5}$$

$$\left|[\alpha_{HAp}]_{X-Y-Z}\right| = \left|\left[\alpha'_{HAp-tsp}\right]_{x-y-z}\right| \tag{S6}$$

References

[S1]   M. Rivas, L. J. del Valle, P. Turon, C. Alemán, J. Puiggalí, *Green Chem.* **2018**, *20*, 685−693.

[S2]   J. S. Anderson, M. W. Roberts, F. S. Stone, Reactivity of solids: Proceedings of the seventh international symposium on the reactivity of solids, Bristol, 17-21 July 1972. Chapman and Hall: London 1972, pp xvii, 812 p.

Table S1. Conditions used for the synthesis of HAp with different degrees of crystallinity (χ_c). The concentration of the $(NH_4)_2HPO_4$ and $Ca(NO_3)_2$ solutions was identical in all cases.

Name	pH	Concentration of Solutions (mM)	χ_c (%)
HAp-A	11	100	74.9±3.4
HAp-B	11	300	64.8±3.1
HAp-C	11	600	75.9±3.5
HAp-D	11	750	64.0±3.6
HAp-E	11.5	500	77.9±2.5

Table S2. Standard deviations obtained for the calcination treatment at 1000 ºC for 30 min, 1 h, 3 h and 5 h.

I_{OH}	A_{OH}	$FWHM_{OH}$	FWHM
0.003	0.001	0.003	0.15
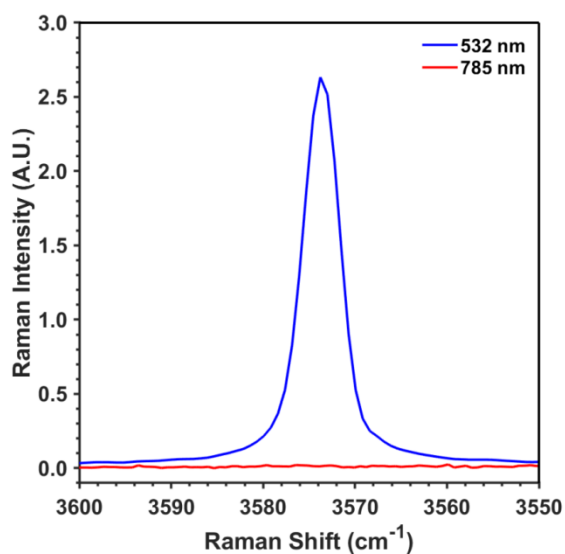
Figure S1. Raman spectra for HAp-1000 sample in the ν-OH region (3550 – 3600 cm^{-1}) recorded with the 785 and 532 nm laser.
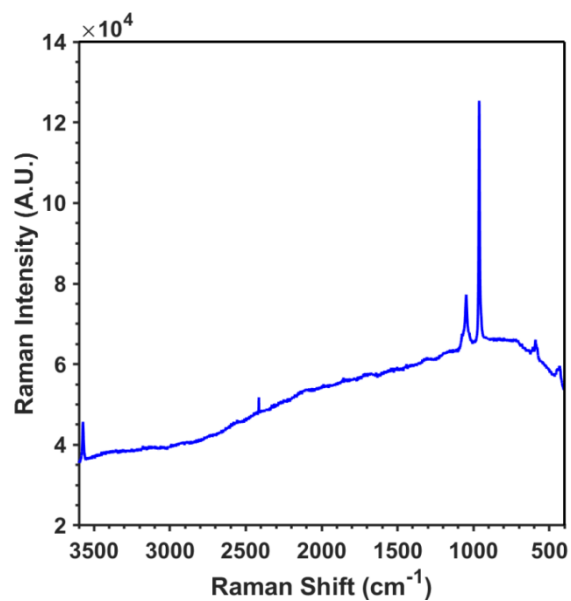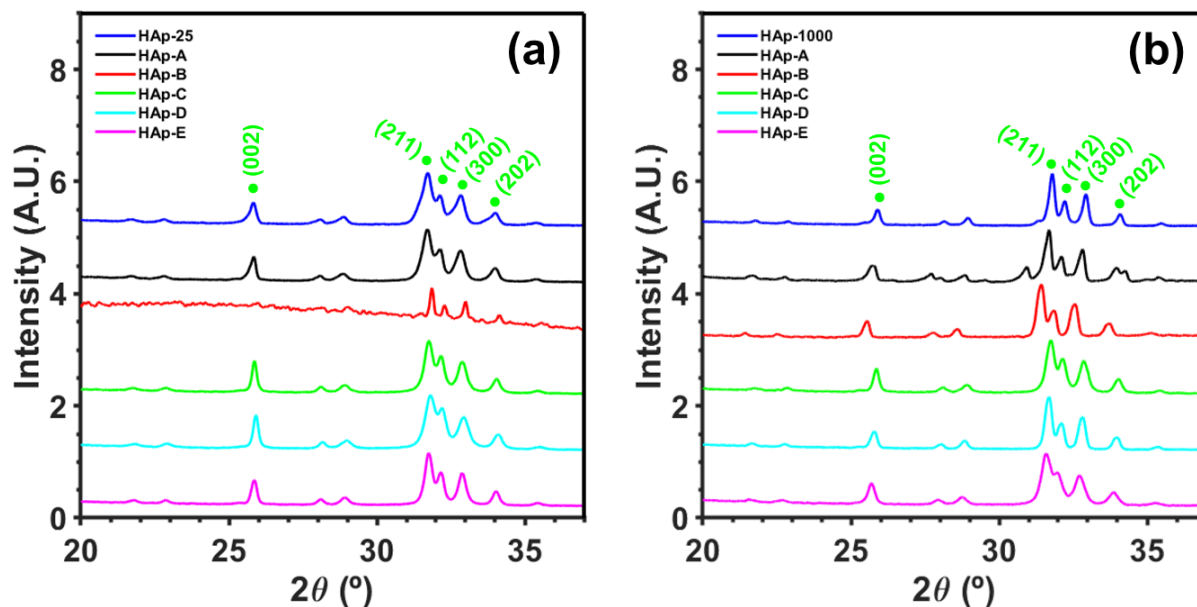
Figure S2. Raw data of the Raman spectrum of HAp-25 sample presenting fluorescence and phosphorescence phenomena recorded at 532 nm. To be compared with the spectrum displayed in Figure 1a, which was recorded at 785 nm.
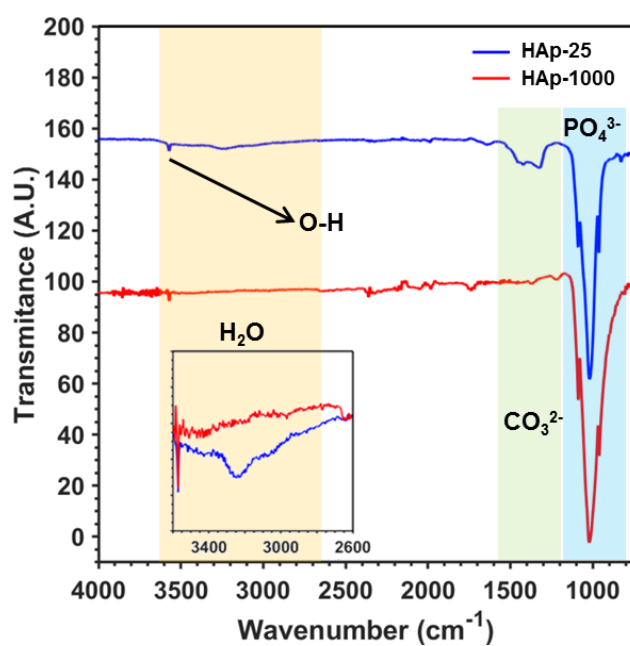

**Figure S3.** FTIR spectra recorded for HAp-25 and HAp-1000 samples.

Figure S4. WAXS spectra of the samples listed in Table S1, used for determining the crystallinity and phase purity: a) non-calcined; and b) calcined at 1000 °C. The spectra of HAp-25 (non-calcined) and HAp-1000 samples have been also included in (a) and (b), respectively. The main reflections of HAp phase have been marked.
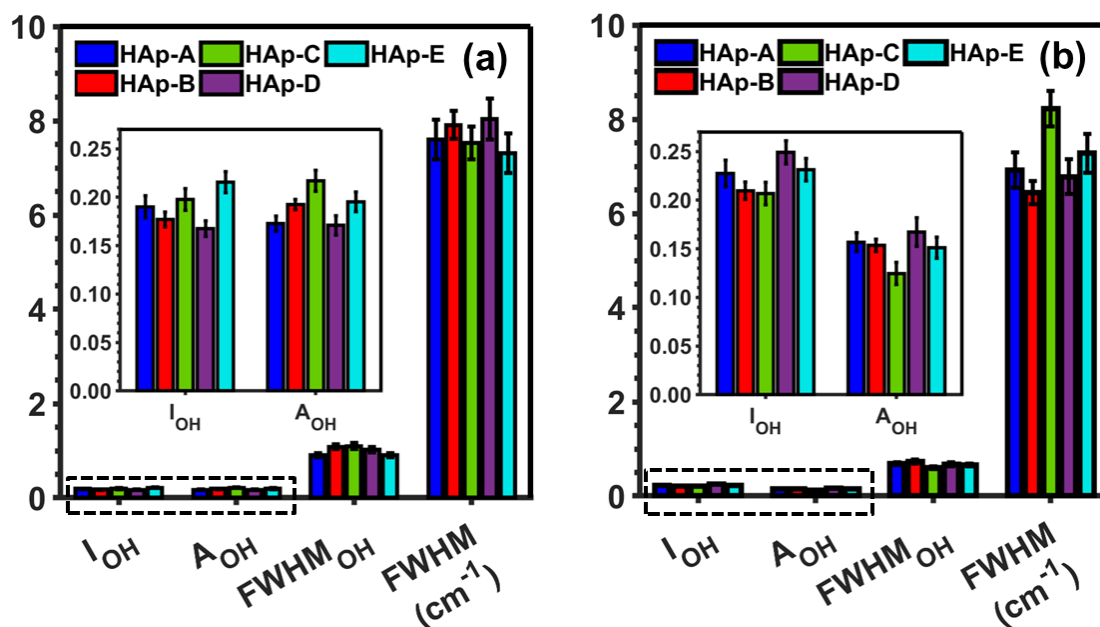

Figure S5. Comparison of the parameters derived from Raman spectroscopy (A_{OH}, I_{OH}, $FWHM_{OH}$ and FWHM) for HAp samples listed in Table S1: (a) non-calcined; and (b) calcined at 1000 °C. The error bars correspond to the standard deviations of three three independent experiments.
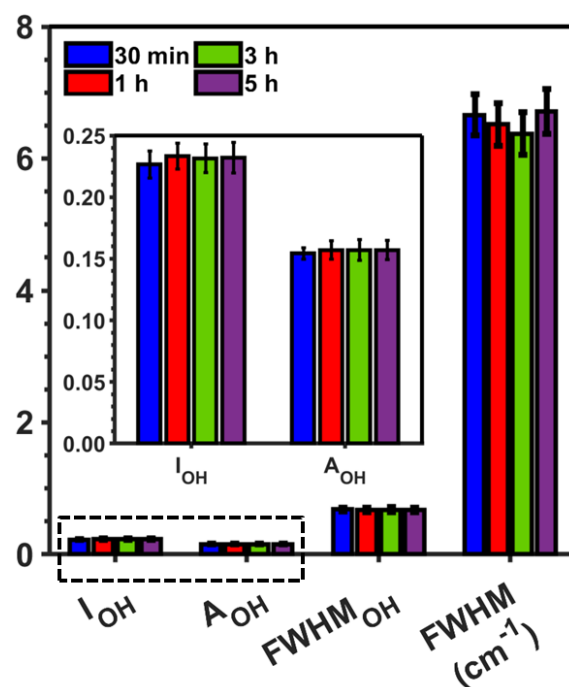
Figure S6. Comparison of the parameters derived from Raman spectroscopy (A_{OH}, I_{OH}, $FWHM_{OH}$ and FWHM) for HAp-1000 samples prepared using different calcination times. The error bars correspond to the standard deviations of three three independent experiments.
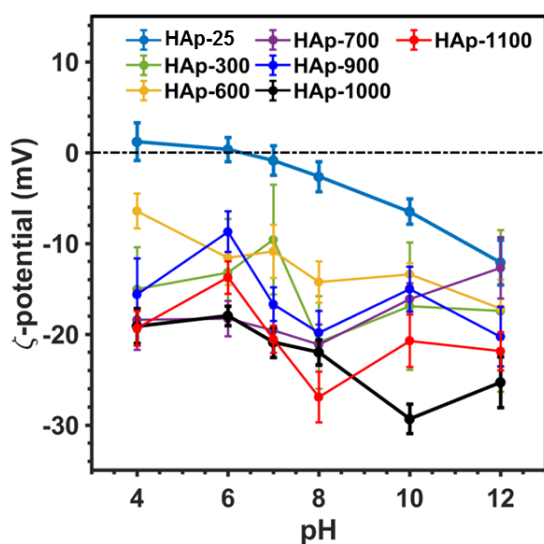
Figure S7. Evolution of the ζ-potential as a function of the pH for non-calcined HAp (HAp-25) and HAp calcined at 300, 600, 700, 900, 1000 and 1100 °C. The error bars correspond to the standard deviations of three three independent experiments.
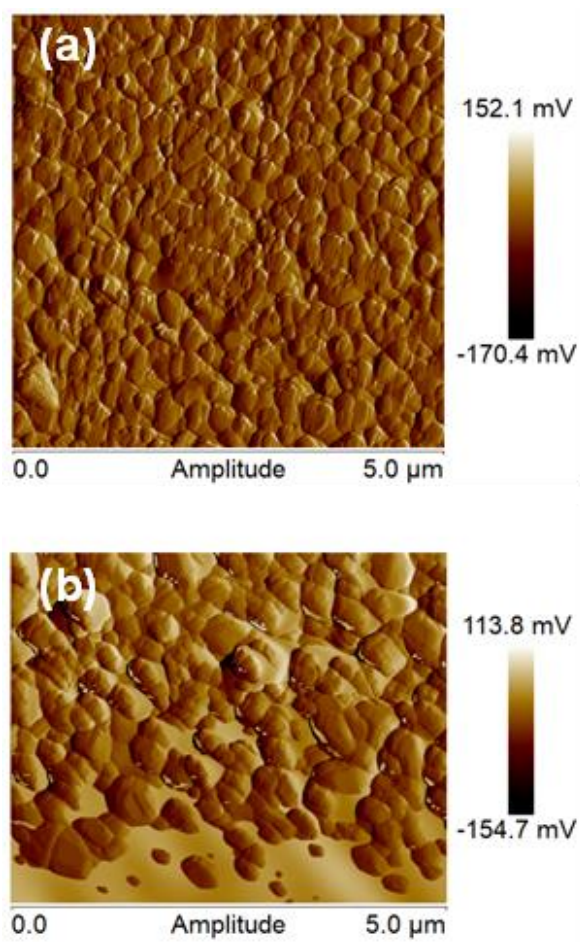
Figure S8. 2D amplitude AFM images of (a) HAp-1000 (5×5 µm^2) and (b) HAp-1000-S (5×4 µm^2) pellets.